ARTICLE

Check for updates

Driving force and nonequilibrium vibronic dynamics in charge separation of strongly bound electron–hole pairs

Alejandro D. Somoza [1,2]✉, Nicola Lorenzoni [1], James Lim[1], Susana F. Huelga [1] & Martin B. Plenio [1]✉

Electron-hole pairs in organic photovoltaics efficiently dissociate although their Coulomb-binding energy exceeds thermal energy at room temperature. The vibronic coupling of electronic states to structured vibrational environments containing multiple underdamped modes is thought to assist charge separation. However, non-perturbative simulations of such large, spatially extended, electronic-vibrational (vibronic) systems remain an unmet challenge which current methods bypass by considering effective one-dimensional Coulomb potentials or unstructured environments where the effect of underdamped modes is ignored. Here we address this challenge with a non-perturbative simulation tool and investigate the charge separation dynamics in one, two and three-dimensional donor-acceptor networks to identify under what conditions underdamped vibrational motion induces efficient long-range charge separation. The resulting comprehensive picture of ultrafast charge separation differentiates electronic or vibronic couplings mechanisms for a wide range of driving forces and identifies the role of entropic effects in extended systems. This provides a toolbox for the design of efficient charge separation pathways in artificial nanostructures.

[1] Institute of Theoretical Physics and IQST, Universität Ulm, Albert-Einstein-Allee 11, D-89069 Ulm, Germany. [2] German Aerospace Center (DLR), Institute of Engineering Thermodynamics, Wilhelm-Runge Straße 10, 89081 Ulm, Germany. ✉email: alejandro.somoza@dlr.de; martin.plenio@uni-ulm.de

When a solar cell made out of an inorganic semiconductor like silicon is exposed to light, electrons can be readily extracted from the valence band to the conduction band and then captured at the electrodes. If, however, light is absorbed by carbon-based materials, photons produce strongly bound electron–hole pairs called excitons, which are collective optical excitations that may be delocalized across several molecular units[1]. In a Frenkel exciton, electron and hole belong, respectively, to the lowest unoccupied molecular orbital (LUMO) and the highest occupied one (HOMO) of the same molecule. In contrast, Wannier-Mott excitons have a charge-transfer (CT) character and the electron and hole pair are separated across several molecular units. The dissociation of excitons is required in order to produce a current[2], and thus the transition between Frenkel excitons and CT states is necessary to describe the dynamics of electron transfer in molecular systems[3]. In photosynthetic organisms excitons are split in pigment-protein complexes called reaction centers[4,5]. In organic photovoltaics (OPV), blends of materials with different electron affinities are used to provide an energetic landscape that is favorable to charge separation at the interface[6]. These devices exhibit ultrafast, long-range charge separation with high quantum efficiencies[7–9]. This means that a large proportion of the absorbed photons produces excitons or strongly bound CT states that are successfully dissociated. Some of these electron–hole pairs however thermalize towards the lowest-energy CT state localized at the interface, which is for this reason considered an energetic trap that leads to non-radiative electron–hole recombination[10–13], as schematically shown in Fig. 1a. This localization process is predominantly mediated by high-frequency vibrational modes that can bridge the energy gap between high-lying exciton/CT states and the lowest-energy interfacial CT state. The energy loss associated with this process is typically larger than 0.6 eV per photon[14–16], leading to a low power conversion efficiency in OPV with respect to their inorganic counterparts that results in a small open circuit voltage[17]. Although energetically costly, dissociation of strongly bound electron–hole pairs[8,9] takes place despite the much lower thermal energy at room temperature. The energy of bound CT states is largely dependent on the offset between the LUMO of the acceptor and the HOMO of the donor[18,19]. Fixing the acceptor and employing different donor materials (or vice versa) is a popular strategy to investigate the energetics at the interface and

achieve a high voltage, small energy losses and sufficient photocurrent density[17,20–23]. Surprisingly, some of these blends show ultrafast and efficient exciton dissociation despite having small or no apparent driving force[13,16,24–30]. The driving force is a crucial parameter in charge separation and refers to the energy difference between exciton and interfacial CT state (see Δ in Fig. 1a). Hybridization between exciton and CT states has been thought to be behind the successful ultrafast charge separation of these promising materials, which are often based on small molecules (oligomers) with acceptor-donor–acceptor structures that have reached power conversion efficiencies of up to 17%[13,26,31,32]. This represents an astonishing 50% increase in the state-of-the-art performance of organic photovoltaics in less than a decade.

From finite molecular clusters to periodic molecular solids, ultrafast long-range charge separation has appeared across a wide variety of photovoltaic platforms, but the underlying mechanism has not been understood fully, leading some to advocate for a deeper analysis of charge separation processes[33,34]. Some experimental studies rule out thermal activation as an important mechanism for charge separation in a large number of photovoltaic devices[35–37]. In contrast, the vibronic coupling to underdamped vibrational modes is presumed to enable coherent charge separation[38–43], which requires non-perturbative simulation tools for a reliable description of the vibronic interaction between exciton/CT states and molecular vibrations. These long-lived intramolecular high-frequency modes typically correspond to carbon-carbon stretch bonds with a period of ~20 fs and may have vibrational lifetimes on a picosecond scale[38,39,44]. However, in many theoretical studies on the charge separation in extended systems, a broad and unstructured environmental spectral density has been considered[45–47] to reduce simulation costs, neglecting the ubiquitous presence of underdamped vibrational modes in organic molecules and their role in charge separation. In addition, the non-Markovian vibronic effects proposed to suppress the localization of electron–hole pairs at the interfaces, e.g. suggested in ref. [47], are found to be well described by a Markovian quantum master equation, as shown in Supplementary Note 1, due to weak vibronic coupling strength and no underdamped modes considered in simulations. This indicates that a vibronic mechanism inferred solely on the basis of non-perturbative numerical results without the subsequent formulation of an accurate physical mechanism may lead to ambiguities in the interpretation of the
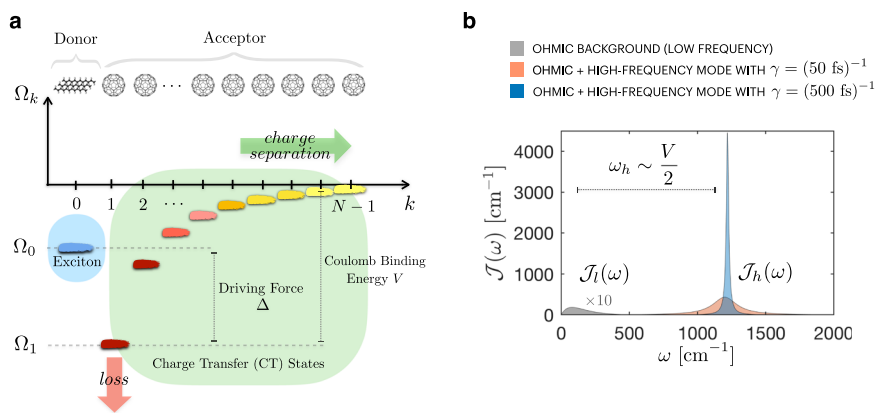

Fig. 1 Coulomb potential and vibrational environments. a Schematic representation of a one-dimensional chain consisting of a donor and (N−1) acceptors. The Coulomb binding energy of electron and hole is modeled by $\Omega_k = -V/k$ with $V = 0.3$ eV for $k \geq 1$. The energy gap between exciton and interfacial CT states is defined as driving force $\Delta = \Omega_0 - \Omega_1$. **b** Vibrational environments consist of low-frequency phonon baths with room temperature energy scales ($k_B T \approx 200$ cm^{-1}) and high-frequency vibrational modes. In this work, the low-frequency phonons are modeled by an Ohmic spectral density $\mathcal{J}_l(\omega)$ with an exponential cutoff, while the high-frequency modes are described by Lorentzian spectral densities $\mathcal{J}_h(\omega)$ centered at vibrational frequency $\omega_h = 1200$ cm^{-1} (or 1500 cm^{-1}). The vibrational damping rate of the high-frequency modes is taken to be $\gamma = (50\,\text{fs})^{-1}$ or $(500\,\text{fs})^{-1}$, as shown in red and blue, respectively, to investigate the role of non-equilibrium vibrational motion in long-range charge separation.

underlying mechanism. Some first-principles numerical methods have been employed to simulate vibronic charge separation[48–55], where underdamped vibrational modes are considered. However, the interpretation of simulated results is a non-trivial issue here. For instance, in ref. [48], an effective one-dimensional Coulomb potential is considered where electron–hole binding energy is assumed to be reduced by instantaneous electron delocalization in three-dimensional acceptor aggregates and as a result the electronic coupling being responsible for a hole transfer becomes larger in magnitude than the detunings in energy levels of the effective potential. In Supplementary Note 2, we show how, in this case, deactivating completely the vibrational environment has little impact on charge separation dynamics. This leads us to conclude that the ultrafast long-range charge separation observed in ref. [48] is not necessarily enhanced by vibronic couplings, but merely induced by the weak Coulomb binding energy. Other theoretical studies have focused on intermolecular modes as the relevant vibrations behind charge separation[56], while sometimes, intramolecular modes are attributed a hampering role[57]. This is, as we will demonstrate, in sharp contrast to our findings, as intramolecular modes can induce both effects.

In the present work, we discern the underlying mechanisms of charge separation dynamics as a function of the driving force or the structure of vibrational environments and determine under which conditions underdamped vibrational motion induces efficient long-range charge separation in the presence of strong Coulomb binding energy $V \sim 0.3$ eV. To this end we consider one, two and three-dimensional donor–acceptor networks, instead of effective one-dimensional Coulomb potentials, by using our non-perturbative simulation method called dissipation-assisted matrix product factorization (DAMPF)[58–61], to investigate how coherent vibronic couplings promote long-range charge separation in high-dimensional multi-site systems. We show that there are two available mechanisms for ultrafast long-range charge separation in donor–acceptor interfaces. For low driving forces $\Delta \sim 0.15$ eV, the transitions between near-resonant exciton and delocalized CT states occur on a sub-ps time scale even if vibronic couplings are not considered. For high driving forces $\Delta \sim 0.3$ eV, the vibronic coupling of underdamped high-frequency vibrational modes with frequencies $\omega_h \sim 0.15$ eV induces the transitions between exciton and CT states delocalized over multiple acceptors. Here a vibrationally cold exciton can interact resonantly with vibrationally hot lower-energy CT states and, subsequently, also with vibrationally cold high-energy CT states. The charge separation process becomes significantly inefficient in this case when vibronic couplings are ignored in simulations, hinting the genuine vibronic effects induced by underdamped vibrational modes. Similar conclusions can be drawn from a vibronic model of pentacene with two electronic states that have been recently put forth[62], where the quantum coherence between local excitons and CT states is shown to strongly depend on specific pathways of vibrational relaxation. For both low and high driving forces, we demonstrate that the time scale of the charge localization towards the donor–acceptor interfaces is determined by the lifetime of the high-frequency vibrational modes, as strongly damped modes promote the transitions to the lowest-energy interfacial CT state. These results demonstrate that experimentally measured long-lived vibrational and vibronic coherences in OPV[38–43] may have a functional relevance in charge separation processes.

Results and discussion

Model. To investigate the influence of underdamped vibrational motion on the charge separation of strongly bound electron–hole pairs, we consider a one-dimensional chain consisting of N sites, composed of an electron donor in contact with a chain of $(N-1)$

electron acceptors, as schematically shown in Fig. 1a. Two and three-dimensional donor–acceptor networks will be considered later. The electronic Hamiltonian is modeled by

$$H_e = \sum_{k=0}^{N-1} \Omega_k |k\rangle \langle k| + \sum_{k=0}^{N-2} J_{k,k+1}(|k\rangle \langle k+1| + h.c.), \quad (1)$$

where $h.c.$ denotes the Hermitian conjugate. Here $|0\rangle$ denotes an exciton state localized at the donor, while $|k\rangle$ with $k \geq 1$ is a CT state with an electron localized at the kth acceptor. For simplicity, we assume that the hole is fixed at the donor within the time scale of our simulations due to its lower mobility with respect to the electron[45,47,63]. The energy levels of CT states take into account the Coulomb attraction between electron and hole, given by $\Omega_k = -V/k$ for $k \geq 1$. We choose a value of $V = 0.3$ eV in accordance with numerous estimates of the Coulomb binding energy in the OPV literature[63–66]. We take $J_{k,k+1} = 500$ cm$^{-1} \approx 0.06$ eV for the electronic coupling being responsible for an electron transfer, a common value found in acceptor aggregates such as fullerene derivatives[48,49,67]. The exciton energy Ω_0 depends on the molecular properties of the donor[8,18,19], which will be considered a free variable parametrized by the driving force $\Delta = \Omega_0 - \Omega_1$, as shown in Fig. 1a.

For simplicity, we assume that each electronic state $|k\rangle$ is coupled to an independent vibrational environment that is initially in a thermal state at room temperature. The vibrational Hamiltonian is written as

$$H_\nu = \sum_{k=0}^{N-1} \sum_q \omega_q b_{k,q}^\dagger b_{k,q}, \quad (2)$$

with $b_{k,q}$ ($b_{k,q}^\dagger$) describing the annihilation (creation) operator of a vibrational mode with frequency ω_q that is locally coupled to the electronic state $|k\rangle$. The vibronic interaction is modeled by

$$H_{e-\nu} = \sum_{k=0}^{N-1} |k\rangle \langle k| \sum_q \omega_q \sqrt{s_q}(b_{k,q} + b_{k,q}^\dagger), \quad (3)$$

where the vibronic coupling strength is quantified by the Huang-Rhys (HR) factors s_q. The vibrational environments are fully characterized by a phonon spectral density $\mathcal{J}(\omega) = \sum_q \omega_q^2 s_q \delta(\omega - \omega_q)$ with $\delta(\omega)$ denoting the Dirac delta function. According to first-principles calculations of functionalized fullerene electron acceptors[31,68–70], the vibrational environment consists of multiple low-frequency modes, with vibrational frequencies smaller than the thermal energy at room temperature ($k_B T \approx 200$ cm$^{-1} \approx 0.025$ eV), and a few discrete modes with high vibrational frequencies of the order of ~ 1000 cm^{-1} and HR factors $\lesssim 0.1$. Motivated by these observations, we consider a phonon spectral density $\mathcal{J}(\omega) = \mathcal{J}_l(\omega) + \mathcal{J}_h(\omega)$ where $\mathcal{J}_l(\omega) = \frac{\lambda_l}{\omega_l} \omega e^{-\omega/\omega_l}$, with $\omega_l = 80$ cm^{-1} and $\lambda_l = 50$ cm^{-1}, describes a low-frequency phonon spectrum (see gray curve in Fig. 1b). The high-frequency vibrational modes are modeled by a Lorentzian function $\mathcal{J}_h(\omega) = \frac{4\omega_h s_h \gamma(\omega_h^2 + \gamma^2)}{\pi} \omega((\omega + \omega_h)^2 + \gamma^2)^{-1}((\omega - \omega_h)^2 + \gamma^2)^{-1}$ with vibrational frequency $\omega_h = 1200$ cm$^{-1} \approx V/2 = 0.15$ eV, HR factor $s_h = 0.1$ and damping rate γ. Molecular crystals are thought to exhibit important anharmonicities in some strongly coupled low-frequency modes that may not be properly described by our choice of linear vibronic coupling in the Hamiltonian[69,71,72]. This corresponds to the breakdown of the assumption of Gaussian environments where second moments of creation and annihilation operators completely determine the nature of vibronic interactions. Consequently, we have avoided the use of strongly coupled low-frequency vibrations of frequency $\lesssim 100$ cm^{-1}, where the anharmonic behavior is more pronounced. Instead, we employ a continuous spectral density of the Ohmic type to model the

dissipative effects of a low-frequency vibrational environment at room temperature and focus on the influence that intramolecular, high-frequency modes have on charge separation.

In order to tackle the problem of simulating large vibronic systems, we have extended DAMPF[59], where a continuous vibrational environment is described by a finite number of oscillators undergoing Markovian dissipation (pseudomodes) and a tensor network formalism is used. With DAMPF the reduced electronic system dynamics can be simulated in a numerically accurate manner for highly structured phonon spectral densities by fitting the corresponding bath correlation functions via an optimal set of parameters of either coupled or uncoupled pseudomodes[58–61]. The extended DAMPF method opens the door to non-perturbative simulations of many body systems consisting of several tens of sites coupled to structured environments in one, two- and three spatial dimensions, as will be demonstrated in this work. More details about the method and the explicit equation of motion in terms of pseudomodes can be found in the "Methods" section below.

Driving Force and Vibrational Environments. Here we investigate the charge separation dynamics on a sub-ps time scale simulated by DAMPF. For simplicity, we consider a linear chain consisting of a donor and nine acceptors ($N = 10$). Longer one-dimensional chains and higher-dimensional donor/acceptor networks will be considered later. We assume that an exciton state $|0\rangle$ localized at the donor site is created at the initial time $t = 0$ and then an electron transfer through the acceptors induces the transitions from the exciton to the CT states $|k\rangle$ with $k \geq 1$. The mean distance between electron and hole is considered a figure of merit for charge separation, defined by $\langle x(t) \rangle = \sum_{k=0}^{N-1} k P_k(t)$ with $P_k(t)$ representing the populations of the exciton and CT states $|k\rangle$ at time t, with the assumption that the distance between nearby sites is uniform. To investigate how the initial charge separation dynamics depends on the exciton energy Ω_0 and the structure of vibrational environments, we analyze in Fig. 2 the time-averaged electron–hole distance, defined by $\langle x \rangle_{t \leq T} = \frac{1}{T} \int_0^T dt \langle x(t) \rangle$ with $T = 400$ fs, as a function of the driving force $\Delta = \Omega_0 + V$ for various environmental structures. As evidenced by the dynamics of the populations in Figs. 3 and 4, an integration interval of $T = 400$ fs is sufficient to differentiate between various rates of vibrational relaxation and their influence on charge separation. Nonetheless, the duration of nonequilibrium dynamics can extend up to the picosecond scale for sufficiently long-lived vibrational modes. The role of high-frequency vibrational modes and their nonequilibrium motion in charge separation processes is identified by considering (i) no environments ($\mathcal{J}(\omega) = 0$), (ii) low-frequency phonon baths ($\mathcal{J}(\omega) = \mathcal{J}_l(\omega)$, see gray curve in Fig. 1b), (iii) high-frequency vibrational modes with controlled damping rates $\gamma \in \{(50\,\text{fs})^{-1}, (500\,\text{fs})^{-1}\}$ ($\mathcal{J}(\omega) = \mathcal{J}_h(\omega)$, see red and blue curves in Fig. 1b), and (iv) the total vibrational environments including both low-frequency phonon baths and high-frequency vibrational modes ($\mathcal{J}(\omega) = \mathcal{J}_l(\omega) + \mathcal{J}_h(\omega)$).

In Fig. 2a, the time-averaged electron–hole distance is shown as a function of the driving force Δ when vibrational environments are not considered ($\mathcal{J}(\omega) = 0$). In this case, the charge separation dynamics is purely electronic and the mean electron–hole distance shows multiple peaks for $\Delta \lesssim 0.3$ eV. When electronic states are only coupled to low-frequency phonon baths ($\mathcal{J}(\omega) = \mathcal{J}_l(\omega)$), these peaks are smeared out, resulting in a smooth, broad single peak centered around $\Delta_e \approx 0.15$ eV. The origin and structure of these electronic resonances will be explained in detail in the next section. In Fig. 2b where the electronic states are coupled to high-frequency vibrational modes ($\mathcal{J}(\omega) = \mathcal{J}_h(\omega)$), the time-averaged electron–hole distance is displayed for different vibrational damping

rates $\gamma = (50\,\text{fs})^{-1}$ and $\gamma = (500\,\text{fs})^{-1}$, shown in red and blue, respectively. With ω_h denoting the vibrational frequency of the high-frequency modes, the electron–hole distance is maximized at $\Delta_e \approx 0.15$ eV, $\Delta_e + \omega_h \approx 0.3$ eV, $\Delta_e + 2\omega_h \approx 0.45$ eV, making the charge separation process efficient for a broader range of the driving force Δ when compared to the cases that the high-frequency modes are ignored (see Fig. 2a). It is notable that the electron–hole distance is larger for the lower damping rate $\gamma = (500\,\text{fs})^{-1}$ of the high-frequency vibrational modes than for the higher damping rate $\gamma = (50\,\text{fs})^{-1}$. These results imply that nonequilibrium vibrational dynamics can promote long-range charge separation. This observation still holds even if the low-frequency phonon baths are considered in addition to the high-frequency vibrational modes ($\mathcal{J}(\omega) = \mathcal{J}_l(\omega) + \mathcal{J}_h(\omega)$), as shown in Fig. 2c, where the electron–hole distance is maximized at $\Delta_e \approx 0.15$ eV and $\Delta_v = \Delta_e + \omega_h \approx 0.3$ eV. We note that the electron–hole distance at low driving forces $\Delta \sim \Delta_e$ is insensitive to the presence of vibrational environments, while at high driving forces $\Delta \sim \Delta_v$, the charge separation process becomes significantly inefficient when the high-frequency vibrational modes are ignored. These results suggest that vibrational environments may play an essential role in the long-range charge separation at high driving forces, while the exciton dissociation at low driving forces may be governed by electronic interactions.

So far the time-averaged mean electron–hole distance has been considered to identify under what conditions the charge separation on a sub-ps time scale becomes efficient. However, it does not show how much populations of the CT states with well-separated electron–hole pairs are generated and how quickly the long-range electron–hole separation takes place. In Fig. 3, we show the population dynamics of the CT states where electron and hole are separated more than four molecular units, defined by $\sum_{k=5}^{9} P_k(t)$, for the case that electronic states are coupled to the total vibrational environments ($\mathcal{J}(\omega) = \mathcal{J}_l(\omega) + \mathcal{J}_h(\omega)$). When the high-frequency vibrational modes are weakly damped with $\gamma = (500\,\text{fs})^{-1}$, the electron is transferred to the second half of the acceptor chain within 100 fs and then the long-range electron–hole separation is sustained on a sub-ps time scale for a wide range of the driving forces Δ, as shown in Fig. 3a. When the high-frequency modes are strongly damped with $\gamma = (50\,\text{fs})^{-1}$, for low driving forces around $\Delta_e \approx 0.15$ eV the long-range charge separation occurs within 100 fs, but the electron is quickly transferred back to the donor–acceptor interface, as shown in Fig. 3b. For high driving forces around $\Delta_v \approx 0.3$ eV, the long-range charge separation and subsequent localization towards the interface take place on a slower time scale when compared to the case of the low driving forces. These results demonstrate that underdamped vibrational motion can promote long-range charge separation when the excess energy $\Delta - V$, defined by the energy difference between exciton state and fully separated free charge carriers, is negative or close to zero[28–30,73,74].

Electronic mixing at low driving forces. The long-range charge separation observed in DAMPF simulations can be rationalized by analyzing the energy levels and delocalization lengths of the exciton and CT states. In Fig. 2d, we consider the eigenstates $|E_\alpha^{(\text{CT})}\rangle$ of the electronic Hamiltonian where the exciton state $|0\rangle$ and its coupling $J_{0,1}$ to the CT states are ignored, namely $H_{\text{CT}} = \sum_{k=1}^{N-1} \Omega_k |k\rangle\langle k| + \sum_{k=1}^{N-2} J_{k,k+1}(|k\rangle\langle k+1| + h.c.)$. With a hole fixed at the donor site, the probability distributions $|\langle k|E_\alpha^{(\text{CT})}\rangle|^2$ for finding an electron at the kth acceptor site is displayed, which are vertically shifted by $E_\alpha^{(\text{CT})} + V$ with $E_\alpha^{(\text{CT})}$ representing the eigenvalues of H_{CT}. The lowest-energy CT eigenstate is mainly localized at the interface due to the strong Coulomb binding energy considered in simulations ($\Omega_2 - \Omega_1 =$
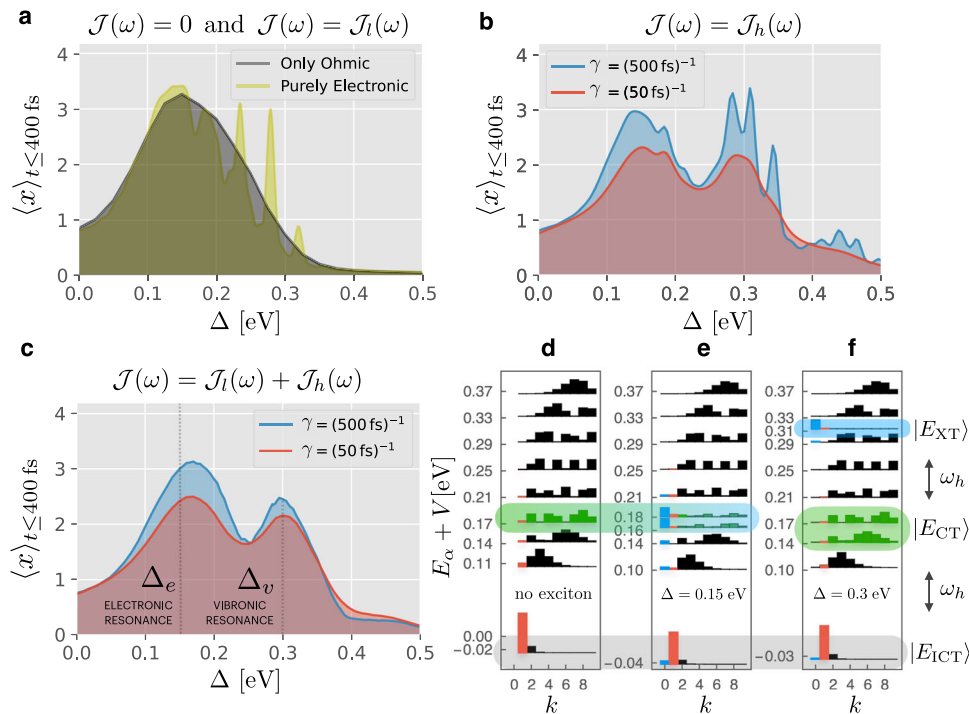
Fig. 2 Charge separation under different vibrational environments and electronic eigenstate structures. a Time-averaged mean electron–hole distance $\langle x \rangle_{t \leq 400\,\text{fs}}$ is displayed as a function of driving force Δ when vibrational environments are absent ($\mathcal{J}(\omega) = 0$) or only low-frequency phonon baths are present ($\mathcal{J}(\omega) = \mathcal{J}_l(\omega)$), shown in yellow and gray, respectively. Here we consider a linear chain consisting of a donor and nine acceptors ($N = 10$ sites). **b, c** Time-averaged mean electron–hole distance when electronic states are coupled to **b** high-frequency vibrational modes only ($\mathcal{J}(\omega) = \mathcal{J}_h(\omega)$) or to **c** the total vibrational environments ($\mathcal{J}(\omega) = \mathcal{J}_l(\omega) + \mathcal{J}_h(\omega)$). Here the vibrational damping rate of the high-frequency modes with frequency $\omega_h = 1200\,\text{cm}^{-1}$ is taken to be $\gamma = (50\,\text{fs})^{-1}$ or $(500\,\text{fs})^{-1}$, shown in red and blue, respectively. **d** Electronic eigenstates of the acceptor when the exciton $|0\rangle$ is electronically decoupled from acceptor sites $|k\rangle$ with $k > 0$. The probability distributions for finding an electron at the kth acceptor are vertically shifted depending on electronic energy levels E_α. **e, f** Electronic eigenstates of the electronically coupled donor–acceptor system where the driving force is taken to be **e** $\Delta_e = 0.15$ eV or **f** $\Delta_v = 0.3$ eV. We employ the notation $|E_{\text{XT}}\rangle \sim |0\rangle$ to refer to eigenstates with an excitonic character, $|E_{\text{CT}}\rangle$ is a charge-transfer (CT) state delocalized over the acceptor and $|E_{\text{ICT}}\rangle \sim |1\rangle$ is another CT state localized at the interface. In (**e**), hybrid exciton-CT states contributing to initial charge separation dynamics are colored in blue/green. In **f**, the exciton and delocalized CT states, governing initial charge separation via a vibronic mixing, are highlighted in blue and green, respectively. In (**d**–**f**), the probabilities for finding an electron at donor/acceptor interface are shown in red.
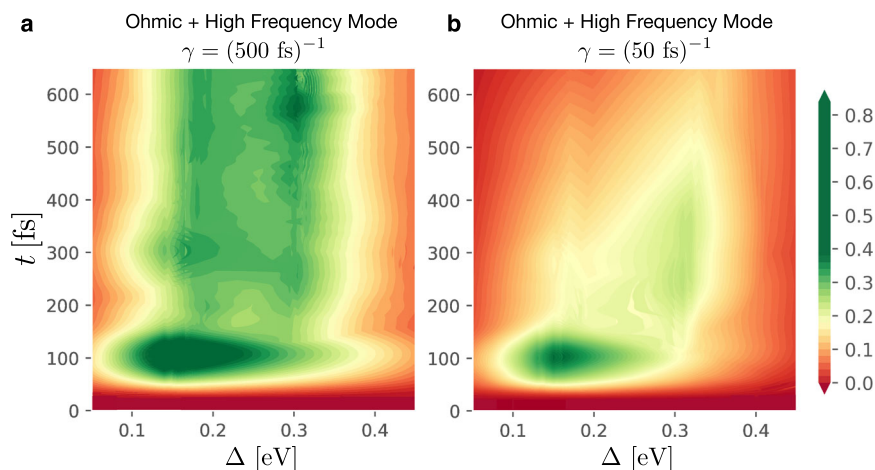

Fig. 3 Long-range charge separation dynamics. a, b Total probability for separating an electron–hole pair more than four molecular units, $\sum_{k=5}^{9} P_k(t)$, is shown as a function of time t and driving force Δ. The colorbar quantifies the sum of probabilities $\sum_{k=5}^{9} P_k(t)$ and can be thought as a measure of the probability of successful charge separation. Here a linear chain consisting of $N = 10$ sites is considered where electronic states are coupled to total vibrational environments ($\mathcal{J}(\omega) = \mathcal{J}_l(\omega) + \mathcal{J}_h(\omega)$). The damping rate of the high-frequency modes with $\omega_h = 1200\,\text{cm}^{-1}$ is taken to be (**a**) $\gamma = (500\,\text{fs})^{-1}$ or (**b**) $\gamma = (50\,\text{fs})^{-1}$.

$V/2 = 0.15$ eV $> J_{1,2} \approx 0.06$ eV). The other higher energy CT eigenstates are significantly delocalized in the acceptor domain with smaller populations $|\langle 1|E_\alpha^{(\text{CT})}\rangle|^2$ at the interface for higher energies $E_\alpha^{(\text{CT})}$, as highlighted in red.

We consider the full electronic Hamiltonian H_e, including now an exciton in the donor with an energy $\Omega_0 = \Omega_2$ that is equal to that of the second acceptor site. This corresponds to a driving force $\Delta_e = V/2 = 0.15$ eV, that is half the value of the Coulomb
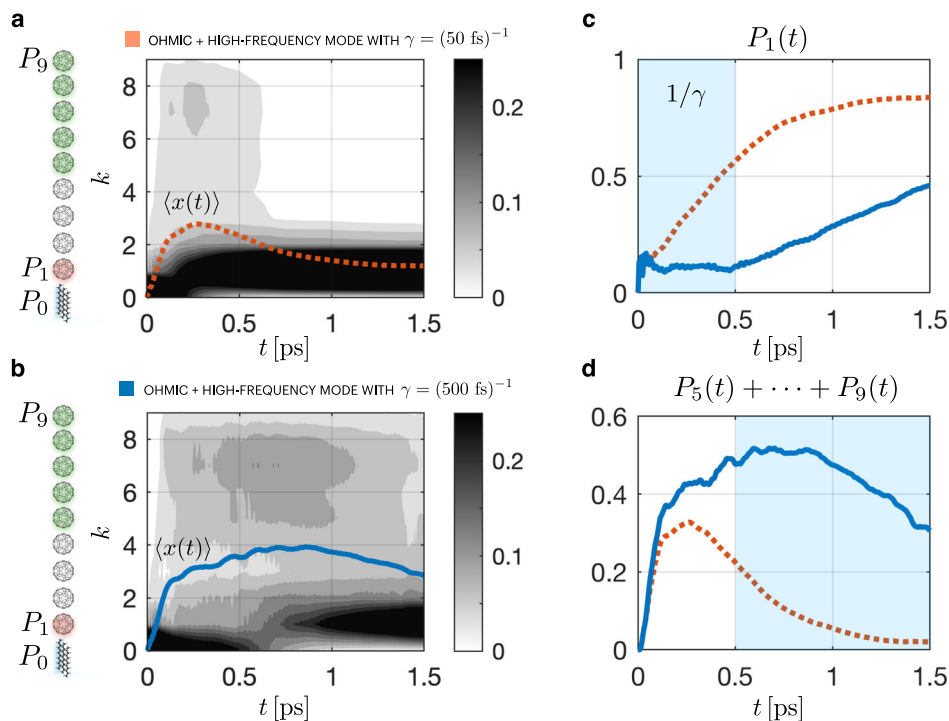
Fig. 4 Vibration-assisted exciton dissociation and charge localization towards donor/acceptor interfaces. a With a hole fixed at donor, the probability distribution for finding an electron at the donor ($k = 0$, corresponding to exciton) or at the kth acceptor ($k \geq 1$) is displayed as a function of time t, with mean electron–hole distance $\langle x(t) \rangle$ shown in red (the colorbar quantifies these probabilities). We remark that $k \in [0, N-1]$ is a discrete variable, and the continuous nature of the contour plot emerges when displaying curves of equal populations that are extracted from the time-series data. With high driving force $\Delta_v = 0.3$ eV, here we consider a linear chain consisting of $N = 10$ sites and total vibrational environments ($\mathcal{J}(\omega) = \mathcal{J}_l(\omega) + \mathcal{J}_h(\omega)$) including strongly damped high-frequency modes with $\omega_h = 1200$ cm^{-1} and $\gamma = (50 \text{ fs})^{-1}$. **b** Charge separation dynamics when the high-frequency vibrational modes are weakly damped with $\gamma = (500 \text{ fs})^{-1}$. **c** Population dynamics of the first acceptor site at the interface, i.e. charge-transfer (CT) state |1⟩. **d** Probability for separating an electron–hole pair more than four molecular units, $\sum_{k=5}^{9} P_k(t)$, shown as a function of time t. In both (**c**, **d**), the strongly (weakly) damped case with $\gamma = (50 \text{ fs})^{-1}$ ($\gamma = (500 \text{ fs})^{-1}$ is shown in red (blue).

binding energy. In Fig. 2a, we observe how efficient long-range charge separation can take place even in the absence of vibrational environments, with a driving force that is far lower than the binding energy of the electron–hole pair. The exciton state |0⟩ is coupled to the eigenstates $\left| E_\alpha^{(CT)} \right\rangle$ of H_{CT} via the electronic coupling $H_i = J_{0,1}(|0\rangle\langle 1| + h.c.)$ at the interface, leading to the exciton-CT couplings in the form $\langle 0 | H_i | E_\alpha^{(CT)} \rangle = J_{0,1} \langle 1 | E_\alpha^{(CT)} \rangle$. This implies that the transition between exciton and CT state $\left| E_\alpha^{(CT)} \right\rangle$ is enhanced when the exciton energy Ω_0 is near-resonant with the CT energy $E_\alpha^{(CT)}$ and the CT state has sufficiently high population $|\langle 1 | E_\alpha^{(CT)} \rangle|^2$ at the interface (see red bars in Fig. 2b). For $\Delta_e = \Omega_0 + V = 0.15$ eV, the exciton state can be strongly mixed with a near-resonant CT state delocalized over multiple acceptor sites (see Fig. 2d), leading to two hybrid exciton-CT eigenstates of the total electronic Hamiltonian H_e, described by the superpositions of |0⟩ and multiple $|k\rangle$ with $k \geq 1$ (see Fig. 2e). This indicates that the multiple peaks in the time-averaged electron–hole distance $\langle x \rangle_{t \leq 400 \text{ fs}}$ shown in Fig. 2a originate from the resonances between exciton and CT states $\left| E_\alpha^{(CT)} \right\rangle$. Here the high-lying CT states with energies $E_\alpha^{(CT)} + V \gtrsim 0.3$ eV do not show long-range electron–hole separation, as the interfacial electronic couplings $J_{0,1} \langle 1 | E_\alpha^{(CT)} \rangle$ are not strong enough to induce notable transitions between exciton and CT states within the time scale $T = 400$ fs considered in Fig. 2a. These high-energy CT states can be populated via a near-resonant exciton state, but the corresponding purely electronic charge separation occurs on a slower ps time

scale, as shown in Supplementary Note 3, and therefore this process can be significantly affected by low-frequency phonon baths. This is contrary to the charge separation at the low driving force $\Delta_e \approx 0.15$ eV, which takes place within 100 fs and therefore the early electronic dynamics is weakly affected by vibrational environments. We note that when this analysis is applied to the charge separation model in ref. [48], it can be shown that an exciton state is strongly mixed with near-resonant CT states delocalized in an effective one-dimensional Coulomb potential and as a result the ultrafast long-range charge separation reported in ref. [48] can be well described by a purely electronic model where vibrational environments are ignored (see Supplementary Note 2).

Vibronic mixing at high driving forces. Contrary to the case of $\Delta_e = 0.15$ eV, the eigenstates of the full electronic Hamiltonian H_e with $\Delta_v = 0.3$ eV show a weak mixing between exciton and CT states, as displayed in Fig. 2f, where the eigenstate $\left| E_{XT} \right\rangle$ with the most excitonic character $|\langle 0 | E_{XT} \rangle| \approx 1$ and marked in blue, has negligible amplitudes $|\langle k | E_{XT} \rangle| \ll 1$ at the acceptor sites with $k > 0$. Here the energy gaps between the exciton state $\left| E_{XT} \right\rangle$, shown in blue, and lower-energy eigenstates $\left| E_{CT} \right\rangle$ with strong CT characters, shown in green, are near-resonant with the vibrational frequency of the high-frequency modes, $E_{XT} - E_{CT} \approx \omega_h$. Therefore, the vibrationally cold exciton state $\left| E_{XT}, 0_v \right\rangle$ can resonantly interact with vibrationally hot CT states $\left| E_{CT}, 1_v \right\rangle$ where one of the high-frequency modes is singly excited. Here the CT states are delocalized in the acceptor domain, but have non-negligible amplitudes around

the interface, leading to a moderate vibronic coupling to the exciton state, $\langle E_{XT}|H_{e-v}|E_{CT}\rangle = \sum_{k=0}^{N-1} \langle E_{XT}|k\rangle\langle k|E_{CT}\rangle \omega_h \sqrt{s_h}(b_{k,h} + b_{k,h}^\dagger)$ with $b_{k,h}$ ($b_{k,h}^\dagger$) denoting the annihilation (creation) operator of the high-frequency vibrational mode locally coupled to electronic state $|k\rangle$. The other high-lying CT states $|E_{CT}'\rangle$ near-resonant with the exciton state, $E_{CT}' \approx E_{XT}$, may have relatively small amplitudes around the interface, so the direct vibronic coupling to the exciton state could be small. However, the transitions from the exciton $|E_{XT}, 0_v\rangle$ to the vibrationally hot low-lying CT states $|E_{CT}, 1_v\rangle$ can allow subsequent transitions to vibrationally cold high-lying CT states $|E_{CT}', 0_v\rangle$, as the delocalized CT states $|E_{CT}\rangle$ and $|E_{CT}'\rangle$ are spatially overlapped. Such consecutive transitions are mediated by vibrational excitations and can delay the process of charge localization at donor–acceptor interfaces if the damping rate of the high-frequency vibrational modes is sufficiently lower than the transition rates amongst exciton and CT states. This picture is in line with the vibronic eigenstate analysis where the high-frequency modes are included as a part of system Hamiltonian in addition to the electronic states, as summarized in Supplementary Note 4.

Functional relevance of long-lived vibrational motion. So far we have discussed the underlying mechanisms behind long-range charge separation on a sub-ps time scale. We now investigate how subsequent charge localization towards the donor–acceptor interface depends on the lifetimes of high-frequency vibrational modes to demonstrate that nonequilibrium vibrational dynamics can maintain long-range electron–hole separation.

In Fig. 4a, b, where the high-frequency modes are strongly and weakly damped, respectively, with $\gamma = (50\,\text{fs})^{-1}$ and $\gamma = (500\,\text{fs})^{-1}$, the population dynamics $P_k(t)$ of the exciton $|0\rangle$ and CT states $|k\rangle$ with $k \geq 1$ is shown as a function of time t up to 1.5 ps in addition to the mean electron–hole distance $\langle x(t)\rangle$. Here we consider the high driving force $\Delta_v = 0.3$ eV where the vibronic transition from exciton $|E_{XT}, 0_v\rangle$ to delocalized CT states $|E_{CT}, 1_v\rangle$ takes place. When the high-frequency modes are strongly damped, the vibrationally hot CT states $|E_{CT}, 1_v\rangle$ quickly dissipate to $|E_{CT}, 0_v\rangle$, leading to subsequent vibronic transitions to vibrationally hot interfacial CT states $|E_{ICT}, 1_v\rangle$ (see Fig. 2f). After that, the vibrational damping of the high-frequency modes generates the population of the lowest-energy interfacial CT state $|E_{ICT}, 0_v\rangle$ and makes the electron–hole pair trapped at the interface, as shown in Fig. 4a. When the high-frequency vibrational modes are weakly damped, the mean electron–hole distance is maximized at ~700 fs, as shown in Fig. 4b, and then the population $P_1(t)$ of the CT state $|1\rangle$ localized around the interface starts to be increased. This localized interfacial state $|1\rangle$ has been considered an energetic trap that leads to non-radiative losses[17]. In Fig. 4c, the population dynamics of $P_1(t)$ is shown in red and blue, respectively, for $\gamma = (50\,\text{fs})^{-1}$ and $\gamma = (500\,\text{fs})^{-1}$. In the strongly damped case, $P_1(t)$ reaches 0.5 in 500 fs and grows up to ~0.8 at 1.5 ps. This is contrary to the weakly damped case where $P_1(t)$ is quickly saturated at ~0.1 within 100 fs and then does not increase until ~500 fs, demonstrating that the charge localization towards the interface can be delayed by the under-damped nature of the high-frequency vibrational modes. The delayed charge localization makes long-range electron–hole separation to be maintained on a picosecond time scale, as shown in Fig. 4d where $\sum_{k=5}^{9} P_k(t)$ is plotted. These results suggest that long-lived vibrational and vibronic coherences observed in nonlinear optical spectra of organic solar cells[39,41,43] may have a functional relevance in long-range charge separation.

Large vibronic systems. So far we have considered a one-dimensional chain consisting of $N = 10$ sites. Here we investigate the charge separation dynamics in larger multi-site systems, including longer linear chains, and donor–acceptor networks in two and three spatial dimensions.

For the linear chains consisting of a donor and $(N - 1)$ acceptors, we consider the total vibrational environments including low-frequency phonon baths and high-frequency vibrational modes with $\gamma = (500\,\text{fs})^{-1}$ ($\mathcal{J}(\omega) = \mathcal{J}_l(\omega) + \mathcal{J}_h(\omega)$). The driving force is taken to be $\Delta_v = 0.3$ eV, for which long-range charge separation occurs mediated by vibronic couplings in the case of $N = 10$ sites. In Fig. 5a, a longer linear chain is considered with $N = 20$ and the population dynamics $P_k(t)$ of the exciton and CT states $|k\rangle$ is shown. It is notable that an electron–hole pair is separated more than ten molecular units within ~200 fs. Interestingly, with a hole fixed at the donor site, the probability distributions $P_k(t)$ for finding an electron at the kth acceptor are strongly delocalized over the entire acceptor chain, which are maximized at $k \approx 6$ and locally minimized at $k \approx 3$. This implies that an exciton state is vibronically mixed with strongly delocalized CT states, as the detunings $\Omega_{k+1} - \Omega_k = V(k(k+1))^{-1}$ in the energy levels of the Coulomb potential become smaller in magnitude than the electronic coupling $J_{k,k+1} = 500\,\text{cm}^{-1}$ being responsible for an electron transfer when $V = 0.3$ eV and $k > 1$. This is in line with the dynamics of the mean electron–hole distance $\langle x(t)\rangle$ of the linear chains consisting of $N \in \{10, 15, 20\}$ sites, shown in solid lines in Fig. 5b, where the exciton dissociation becomes more efficient for longer acceptor chains. The mean electron–hole distance is decreased when the energy levels Ω_k of the Coulomb potential are randomly generated based on independent Gaussian distributions, as the delocalization lengths of the CT states are reduced on average (see Supplementary Note 5). Importantly, for the high driving force $\Delta_v = 0.3$ eV, the charge separation process becomes significantly less efficient when vibrational environments are not considered ($\mathcal{J}(\omega) = 0$), as shown in dashed lines in Fig. 5b. These results suggest that nonequilibrium vibrational dynamics in ordered donor/acceptor aggregates can promote long-range charge separation.

From the perspective of the microcanonical ensemble, the number of charge-separated states becomes much larger than that of interfacial CT states as the dimension of donor–acceptor aggregates is increased[75]. The statistical advantage results in an entropic drive that further promotes charge separation[76] and is relevant in two- and three-dimensional donor–acceptor networks in the thermodynamic limit. To corroborate these ideas, we consider a variety of donor–acceptor networks with different sizes and dimensions. In Fig. 5c, the schematic representations of one-, two- and three-dimensional donor–acceptor networks considered in our simulations are displayed where the size of each network is quantified by the number L of acceptor layers. In the one-dimensional chains, the number of acceptors in each layer is unity, while in the two-dimensional triangular (three-dimensional pyramidal) structures, the number of acceptors in each layer increases linearly (quadratically) as a function of the minimum distance to the donor site. We assume that the distances between nearby sites are uniform and the corresponding nearest-neighbor electron-transfer couplings are taken to be $500\,\text{cm}^{-1}$. The electronic Hamiltonian is described by the exciton and CT states $|k\rangle$ where a hole is fixed at the donor while an electron is localized at the kth acceptor. The corresponding CT energy is modeled by $\Omega_k = -V/|\mathbf{r}_0 - \mathbf{r}_k|$ with $V = 0.3$ eV where $\mathbf{r}_0$ and $\mathbf{r}_k$ denote, respectively, the positions of the donor and kth acceptor with the distance between nearby sites taken to be unity and dimensionless. To increase the size of the donor–acceptor networks that can be
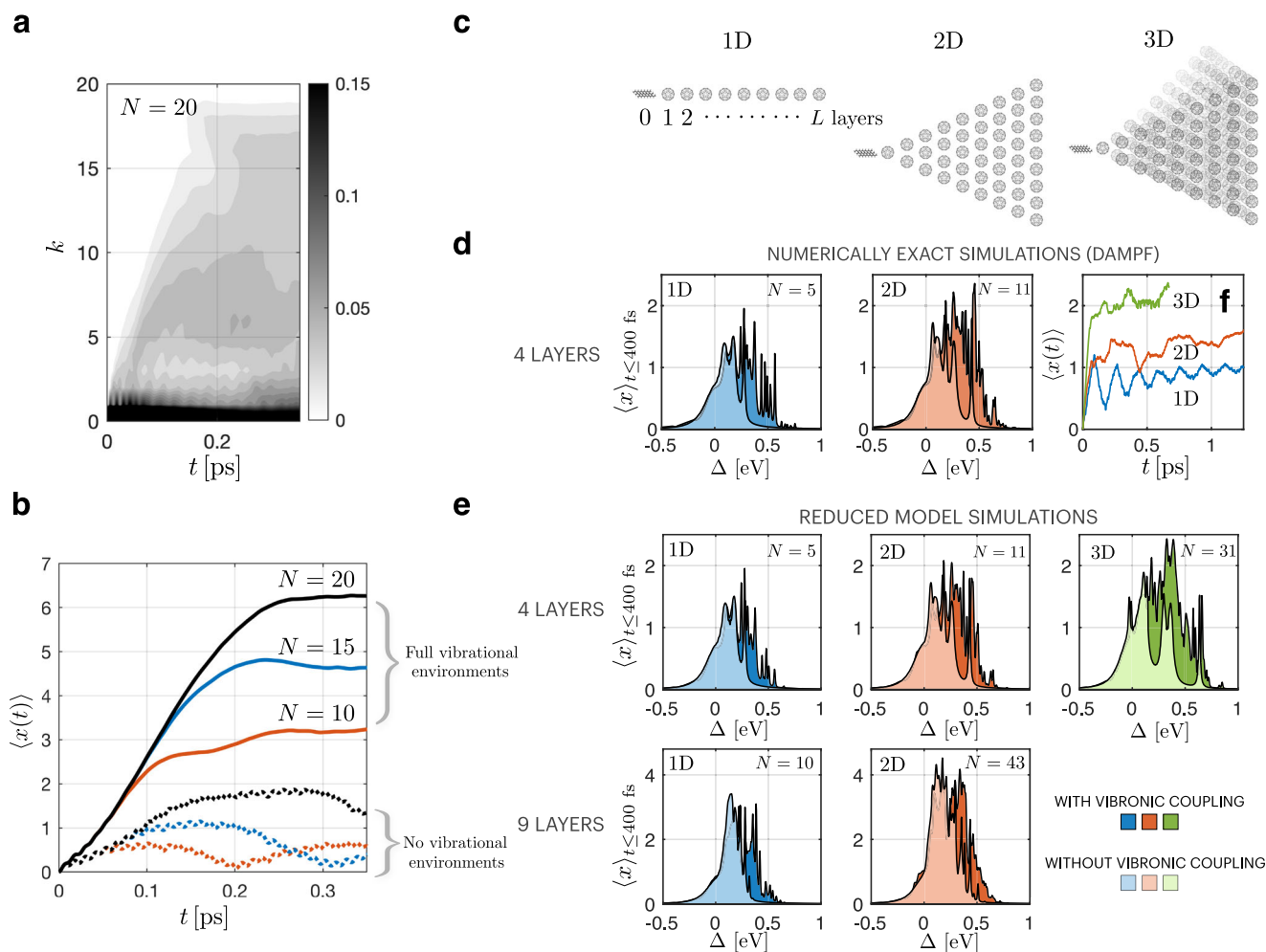
Fig. 5 Charge separation in large vibronic systems in one, two and three spatial dimensions. a With a hole fixed at donor, the probability distribution for finding an electron at the donor ($k = 0$) or at the kth acceptor ($k \geq 1$) is shown as a function of time t for a linear chain consisting of $N = 20$ sites (the colorbar quantifies these probabilities). Here electronic states are coupled to total vibrational environments ($\mathcal{J}(\omega) = \mathcal{J}_l(\omega) + \mathcal{J}_h(\omega)$) including weakly damped high-frequency modes with $\omega_h = 1500\,\mathrm{cm}^{-1}$ and $\gamma = (500\,\mathrm{fs})^{-1}$. **b** Mean electron–hole distances $\langle x(t) \rangle$ of linear chains composed of $N \in \{10, 20, 30\}$ sites, shown in {red, blue, black}, respectively. Here we compare the case of the full environments, shown in solid lines, with that of no vibrational environments ($\mathcal{J}(\omega) = 0$), shown in dashed lines. **c** Schematic representation of one-, two- and three-dimensional donor–acceptor networks where a donor is coupled to acceptor aggregates. **d** Time-averaged mean electron–hole distances $\langle x \rangle_{t \leq 400\,\mathrm{fs}}$ of one- and two-dimensional networks consisting of $L = 4$ acceptor layers, displayed as a function of driving force Δ and computed by the Dissipation-Assisted Matrix Product Factorization method (DAMPF)[59]. Here the case with vibronic coupling to high-frequency modes is shown in blue, red and green for the one-, two- and three dimensional models respectively. The case with no environments is shown in a lighter tone. Note that the overlapped regions indicate that the case without environments is well covered by the vibronic case. **e** Time-averaged mean electron–hole distances of one-, two- and three-dimensional networks consisting of $L = 4$ or $L = 9$ acceptor layers, simulated by a reduced vibronic model (see Supplementary Note 4 for more details). For the three-dimensional network with $L = 4$, $\langle x \rangle_{t \leq 400\,\mathrm{fs}}$ is maximized at high driving forces $\Delta \approx 0.35$ eV. **f** For $\Delta = 0.35$ eV, time evolution of mean electron–hole distance $\langle x(t) \rangle$ is shown for one-, two- and three-dimensional networks with $L = 4$, computed by DAMPF.

considered in simulations, we only consider the high-frequency vibrational modes ($\mathcal{J}(\omega) = \mathcal{J}_h(\omega)$) with $\omega_h = 1500\,\mathrm{cm}^{-1}$, $s_h = 0.1$ and $\gamma = (500\,\mathrm{fs})^{-1}$.

In Fig. 5d, the time-averaged electron–hole distance $\langle x \rangle_{t \leq 400\,\mathrm{fs}}$ simulated by DAMPF is shown as a function of the driving force Δ for one- and two-dimensional networks with $L = 4$. Here we consider the minimum distance between donor and each acceptor layer in the computation of the mean electron–hole distance, instead of the distances between donor and individual acceptors. We compare the case that the high-frequency vibrational modes are coupled to electronic states ($\mathcal{J}(\omega) = \mathcal{J}_h(\omega)$), shown in blue and red for the one-, two-dimensional models respectively, with that of no vibrational environments ($\mathcal{J}(\omega) = 0$), shown in a lighter tone. Note that vibronic couplings make charge separation efficient for a broader range of the driving force Δ in both one-

and two-dimensional networks, and that long-range charge separation is further enhanced in the higher-dimensional network. To simulate larger vibronic systems, in Fig. 5e, we consider a reduced vibronic model constructed within vibrational subspaces describing up to four vibrational excitations distributed amongst the high-frequency vibrational modes in the polaron basis (see Supplementary Note 4 for more details). For $L = 4$, the simulated results obtained by the reduced models of one- and two-dimensional networks are qualitatively similar to the numerically exact DAMPF results shown in Fig. 5d. The reduced model results demonstrate that long-range charge separation can be enhanced by considering a three-dimensional donor–acceptor network with $L = 4$, or by increasing the number of layers to $L = 9$ in the one- and two-dimensional cases. In Fig. 5f, the dynamics of the mean electron–hole distance $\langle x(t) \rangle$ of the one-,

two- and three-dimensional systems with $L = 4$, computed by DAMPF, is shown for a high driving force $\Delta = 0.35$ eV where the time-averaged electron–hole distance of the three-dimensional system shown in Fig. 5e is maximized. These results demonstrate that long-range charge separation can be enhanced by considering higher-dimensional multi-site systems with vibronic couplings.

Conclusions

We have extended the non-perturbative simulation method DAMPF to provide access to charge separation dynamics of a strongly bound electron–hole pair in one-, two- and three-dimensional donor–acceptor networks where a donor is coupled to acceptor aggregates. By controlling the driving force and the structure of vibrational environments, we identified two distinct mechanisms for long-range charge separation. The first mechanism, activated at low driving forces, is characterized by hybrid exciton-CT states where long-range exciton dissociation takes place on a sub-100 fs time scale, which is not assisted by underdamped high-frequency vibrational modes. In the second mechanism, dominating charge separation at high driving forces, the exciton-CT hybridization occurs and it is mediated by vibronic interaction with underdamped high-frequency vibrational modes, leading to efficient charge separation for a broad range of driving forces. For both mechanisms, we have demonstrated that long-range charge separation is significantly suppressed when the high-frequency vibrational modes are strongly damped or delocalization lengths of the CT states are reduced by static disorder in the energy levels of Coulomb potentials. These results suggest that nonequilibrium vibrational motion can promote long-range charge separation in ordered donor–acceptor aggregates.

In some numerical studies, the transition between a Frenkel exciton and a CT state at higher energy is only possible if the vibrational environment is initially excited[62]. In our simulations, all modes start always at equilibrium with their own local and independent environments. The extended nature of our model with a multiplicity of CT states allows us to witness successful charge separation even in the absence of excess vibrational energy. The local exciton in the donor is already energetically close to several CT states that are excited vibrationally. These states lie at the lower part of a band of states that are relatively delocalized over the acceptor and has width of $\sim 2J$. Moreover, no off-diagonal vibronic coupling is necessary to produce these transitions. In the literature on charge separation in OPVs, the term "excess energy" is commonly employed to refer to the energy difference between the LUMO levels of the donor and acceptor ($E_{exc} = \Delta - V$ in our model)[36,65,77]. From our simulations, we conclude that vibrationally hot CT states are important for charge separation in blends with a driving force that is similar in magnitude to the Coulomb binding energy of the electron–hole pair ($\Delta \sim V$). In contrast, charge separation in blends with half the driving force or lower ($\Delta \lesssim V/2$) will be mediated predominantly by purely electronic resonances whose coherence is strongly sensitive to some vibrational relaxation pathways.

The formulation and analysis of a reduced model whose validity became accessible to numerical corroboration thanks to the extension of the numerically exact simulation tool DAMPF allows us to identify unambiguously the mechanisms that underlie charge separation dynamics. The methods employed here can be applied to more realistic models where multiple donors are coupled to acceptor aggregates, without introducing effective one-dimensional Coulomb potentials, and vibrational environments that are highly structured, which deserves a separate investigation. We expect our findings to help open up the engineering of vibrational environments for efficient long-range charge separation in organic solar cells and the identification of charge separation processes in other systems such as photosynthetic reaction centers and other biological processes driven by electron transfer.

Methods

In this work, non-perturbative simulations of charge separation dynamics have been carried out by using dissipation-assisted matrix product factorization (DAMPF) method[59] to take into account non-Markovian effects induced by a continuous spectrum of vibrational environments. The DAMPF method relies on a tensor network formalism and pseudomode theory[58,61], which enables one to consider a finite number of oscillators under Markovian noise (pseudomodes) to mimic in a numerically accurate way the action of the original continuous vibrational environments on reduced electronic system dynamics. In this work, vibrational environments consist of low-frequency phonon baths and high-frequency vibrational modes. The low-frequency phonon bath, modeled by an Ohmic spectral density with an exponential cutoff function, has been described by five pseudomodes coupled to each other. On the contrary, every high-frequency vibrational mode has been described by an independent pseudomode, which can well describe a narrow Lorentzian spectral density. In this case, the vibrational Hamiltonians of the coupled and uncoupled pseudomodes, respectively, are described by

$$H_\nu^{(l)} = \sum_{k=0}^{N-1} \sum_{q=1}^{5} (\omega_q a_{k,q}^\dagger a_{k,q} + g_q a_{k,q} a_{k,q+1}^\dagger + h.c.), \quad (4)$$

$$H_\nu^{(h)} = \sum_{k=0}^{N-1} \omega_h b_{k,h}^\dagger b_{k,h}, \quad (5)$$

where $a_{k,q}$ and $b_{k,h}$ represent pseudomodes coupled to an electronic state $|k\rangle$, and g_q is the coupling between pseudomodes $a_{k,q}$ and $a_{k,q+1}$ with $q+1$ reduced to 1 when $q = 5$. The vibronic couplings to the pseudomodes are described by

$$H_{e-\nu} = \sum_{k=0}^{N-1} |k\rangle\langle k| \sum_{q=1}^{5} (c_q a_{k,q} + c_q^* a_{k,q}^\dagger) \quad (6)$$

$$+ \sum_{k=0}^{N-1} |k\rangle\langle k| \omega_h \sqrt{s_h} (b_{k,h} + b_{k,h}^\dagger). \quad (7)$$

The time evolution of a vibronic density matrix ρ is governed by a Lindblad equation in the form

$$
\begin{aligned}
\dot{\rho} = & -i\big[H_e + H_\nu^{(l)} + H_\nu^{(h)} + H_{e-\nu}, \rho\big] \\
& + \sum_{k=0}^{N-1} \sum_{q=1}^{5} \Big[\gamma_q (n(\omega_q)+1)\Big(a_{k,q}\rho a_{k,q}^\dagger - \tfrac{1}{2}\{a_{k,q}^\dagger a_{k,q}, \rho\}\Big) \\
& + \gamma_q n(\omega_q)\Big(a_{k,q}^\dagger \rho a_{k,q} - \tfrac{1}{2}\{a_{k,q} a_{k,q}^\dagger, \rho\}\Big)\Big] \\
& + \sum_{k=0}^{N-1}\Big[\gamma_h(n(\omega_h)+1)\Big(b_{k,h}\rho b_{k,h}^\dagger - \tfrac{1}{2}\{b_{k,h}^\dagger b_{k,h}, \rho\}\Big) + \gamma_h n(\omega_h)\Big(b_{k,h}^\dagger \rho b_{k,h} - \tfrac{1}{2}\{b_{k,h} b_{k,h}^\dagger, \rho\}\Big)\Big],
\end{aligned}
$$
$$(8)$$

with $n(\omega) = (\exp(\hbar\omega/k_B T) - 1)^{-1}$. The parameters ω_q, g_q, c_q and γ_q of the coupled pseudomodes can be found in Table IV of ref. [61] with a center frequency $\omega_l = 80$ cm^{-1}. The vibrational frequency ω_h of the high-frequency modes is approximately an order of magnitude larger than the thermal energy $k_B T$ at room temperature, for which $n(\omega_h) \ll 1$ and γ_h is reduced to the vibrational damping rate $\gamma \in \{(50\,\text{fs})^{-1}, (500\,\text{fs})^{-1}\}$ considered in the main text.

In DAMPF, where the number of uncoupled (coupled) pseudomodes is denoted by $Q_u = N$ ($Q_c = 5N$), we consider a vibronic density matrix ρ represented in the form

$$\rho = \sum_{k,k'=0}^{N-1} |k\rangle\langle k'| \otimes \sum_{i_1}\sum_{i_2}\cdots\sum_{i_{Q_c}}\sum_{i_{Q_u}} A_{(1;i_1)}^{(k,k')} A_{(2;i_2)}^{(k,k')} \cdots A_{(Q_c;i_{Q_c})}^{(k,k')} A_{(Q_u;i_{Q_u})}^{(k,k')} x_{i_1} \otimes \cdots \otimes x_{i_{Q_u}}, \quad (9)$$

describing a collection of N^2 matrix product states (MPSs), via a vectorization of the density matrix, conditional to the populations $|k\rangle\langle k|$ or coherences $|k\rangle\langle k'|$ with $k \neq k'$ of electronic states $|k\rangle$. This representation retains thus all quantum correlations that have a clear electronic origin, restricting the factorization at the level of different vibrational environments. We found that the simulation costs of DAMPF required to achieve convergence in reduced electronic dynamics are significantly higher for genuine vibronic dynamics occurring at high driving forces $\Delta_\nu \approx 0.3$ eV than for electronic dynamics taking place at low driving forces $\Delta_e \approx 0.15$ eV. This implies that strong correlations between electronic states and vibrational modes, quantified by bond dimensions, occur when a vibronic mixing induces long-range charge separation.

Data availability

The data that support the findings of this study are available from the corresponding author upon reasonable request.

Code availability

The codes used in this work are available from the authors upon reasonable request.

References

1. Scholes, G. D. & Rumbles, G. Excitons in nanoscale systems. *Nat. Mater.* **5**, 920–920 (2006).
2. Hedley, G. J., Ruseckas, A. & Samuel, I. D. W. Light harvesting for organic photovoltaics. *Chem. Rev.* **117**, 796–837 (2017).
3. Coropceanu, V., Chen, X.-K., Wang, T., Zheng, Z. & Brédas, J.-L. Charge-transfer electronic states in organic solar cells. *Nat. Rev. Mater.* **4**, 689–707 (2019).
4. Huelga, S. F. & Plenio, M. B. Vibrations, quanta and biology. *Contemp. Phys.* **54**, 181–207 (2013).
5. Romero, E., Novoderezhkin, V. I. & van Grondelle, R. Quantum design of photosynthesis for bio-inspired solar-energy conversion. *Nature* **543**, 355–365 (2017).
6. Brédas, J.-L., Norton, J. E., Cornil, J. & Coropceanu, V. Molecular understanding of organic solar cells: the challenges. *Acc. Chem. Res.* **42**, 1691–1699 (2009).
7. Park, S. H. et al. Bulk heterojunction solar cells with internal quantum efficiency approaching 100%. *Nat. Photonics* **3**, 297–303 (2009).
8. Clarke, T. M. & Durrant, J. R. Charge photogeneration in organic solar cells. *Chem. Rev.* **110**, 6736–6767 (2010).
9. Gao, F. & Inganäs, O. Charge generation in polymer-fullerene bulk-heterojunction solar cells. *Phys. Chem. Chem. Phys.* **16**, 20291–20304 (2014).
10. Faist, M. A. et al. Competition between the charge transfer state and the singlet states of donor or acceptor limiting the efficiency in polymer:fullerene solar cells. *J. Am. Chem. Soc.* **134**, 685–692 (2011).
11. Nan, G., Zhang, X. & Lu, G. The lowest-energy charge-transfer state and its role in charge separation in organic photovoltaics. *Phys. Chem. Chem. Phys.* **18**, 17546–17556 (2016).
12. Azzouzi, M. et al. Nonradiative energy losses in bulk-heterojunction organic photovoltaics. *Phys. Rev. X* **8**, 31055 (2018).
13. Eisner, F. D. et al. Hybridization of local exciton and charge-transfer states reduces nonradiative voltage losses in organic solar cells. *J. Am. Chem. Soc.* **141**, 6362–6374 (2019).
14. Burke, T. M., Sweetnam, S., Vandewal, K. & McGehee, M. D. Beyond Langevin recombination: how equilibrium between free carriers and charge transfer states determines the open-circuit voltage of organic solar cells. *Adv. Energy Mater.* **5**, 1500123 (2015).
15. Menke, S. M., Ran, N. A., Bazan, G. C. & Friend, R. H. Understanding energy loss in organic solar cells: toward a new efficiency regime. *Joule* **2**, 25–35 (2018).
16. Liu, X., Li, Y., Ding, K. & Forrest, S. Energy loss in organic photovoltaics: nonfullerene versus fullerene acceptors. *Phys. Rev. Appl.* **11**, 024060 (2019).
17. Azzouzi, M., Kirchartz, T. & Nelson, J. Factors controlling open-circuit voltage losses in organic solar cells. *Trends Chem.* **1**, 49–62 (2019).
18. Scharber, M. C. et al. Design rules for donors in bulk-heterojunction solar cells—towards 10 % energy-conversion efficiency. *Adv. Mater.* **18**, 789–794 (2006).
19. Veldman, D., Meskers, S. C. J. & Janssen, R. A. The energy of charge-transfer states in electron donor-acceptor blends: insight into the energy losses in organic solar cells. *Adv. Funct. Mater.* **19**, 1939–1948 (2009).
20. Coffey, D. C. et al. An optimal driving force for converting excitons into free carriers in excitonic solar cells. *J. Phys. Chem. C* **116**, 8916–8923 (2012).
21. Wang, Y. et al. Optical gaps of organic solar cells as a reference for comparing voltage losses. *Adv. Energy Mater.* **8**, 1801352 (2018).
22. Qian, D. et al. Design rules for minimizing voltage losses in high-efficiency organic solar cells. *Nat. Mater.* **17**, 703–709 (2018).
23. Yang, W., Yao, Y., Guo, P., Sun, H. & Luo, Y. Optimum driving energy for achieving balanced open-circuit voltage and short-circuit current density in organic bulk heterojunction solar cells. *Phys. Chem. Chem. Phys.* **20**, 29866–29875 (2018).
24. Zhang, Q. et al. Small-molecule solar cells with efficiency over 9%. *Nat. Photonics* **9**, 35–41 (2015).
25. Jing, L. et al. Fast charge separation in a non-fullerene organic solar cell with a small driving force. *Nat. Energy* **1**, 16089 (2016).
26. Meng, L. et al. Organic and solution-processed tandem solar cells with 17.3% efficiency. *Science* **361**, 1094–1098 (2018).
27. Cui, Y. et al. Over 16% efficiency organic photovoltaic cells enabled by a chlorinated acceptor with increased open-circuit voltages. *Nat. Commun.* **10**, 2515 (2019).
28. Liu, S. et al. High-efficiency organic solar cells with low non-radiative recombination loss and low energetic disorder. *Nat. Photonics* **14**, 300–305 (2020).
29. Zhang, G. et al. Delocalization of exciton and electron wavefunction in non-fullerene acceptor molecules enables efficient organic solar cells. *Nat. Commun.* **11**, 3943 (2020).
30. Zhong, Y. et al. Sub-picosecond charge-transfer at near-zero driving force in polymer:non-fullerene acceptor blends and bilayers. *Nat. Commun.* **11**, 833 (2020).
31. Chen, X.-K., Coropceanu, V. & Brédas, J.-L. Assessing the nature of the charge-transfer electronic states in organic solar cells. *Nat. Commun.* **9**, 5295 (2018).
32. Firdaus, Y. et al. Key parameters requirements for non-fullerene-based organic solar cells with power conversion efficiency >20%. *Adv. Sci.* **6**, 1802028 (2019).
33. Karki, A. et al. Unifying charge generation, recombination, and extraction in low-offset non-fullerene acceptor organic solar cells. *Adv. Energy Mater.* **10**, 2001203 (2020).
34. Alvertis, A. M. et al. Impact of exciton delocalization on exciton-vibration interactions in organic semiconductors. *Phys. Rev. B* **102**, 081122 (2020).
35. Pensack, R. D. & Asbury, J. B. Barrierless free carrier formation in an organic photovoltaic material measured with ultrafast vibrational spectroscopy. *J. Am. Chem. Soc.* **131**, 15986–15987 (2009).
36. Vandewal, K. et al. Efficient Charge Generation by Relaxed Charge-Transfer States at Organic Interfaces. *Nat. Mater.* **13**, 63–68 (2014).
37. Bässler, H. & Köhler, A. "Hot or cold": how do charge transfer states at the donor-acceptor interface of an organic solar cell dissociate? *Phys. Chem. Chem. Phys.* **17**, 28451–28462 (2015).
38. Falke, S. M. et al. Coherent ultrafast charge transfer in an organic photovoltaic blend. *Science* **344**, 1001–1005 (2014).
39. Song, Y., Clafton, S. N., Pensack, R. D., Kee, T. W. & Scholes, G. D. Vibrational coherence probes the mechanism of ultrafast electron transfer in polymer-fullerene blends. *Nat. Commun.* **5**, 4933 (2014).
40. Rafiq, S., Dean, J. C. & Scholes, G. D. Observing vibrational wavepackets during an ultrafast electron transfer reaction. *J. Phys. Chem. A* **119**, 11837–11846 (2015).
41. Sio, A. D. et al. Tracking the coherent generation of polaron pairs in conjugated polymers. *Nat. Commun.* **7**, 13742 (2016).
42. Brédas, J.-L., Sargent, E. H. & Scholes, G. D. Photovoltaic concepts inspired by coherence effects in photosynthetic systems. *Nat. Mater.* **16**, 35–44 (2017).
43. Sio, A. D. et al. Ultrafast relaxation dynamics in a polymer: fullerene blend for organic photovoltaics probed by two-dimensional electronic spectroscopy. *Eur. Phys. J. B* **91**, 236 (2018).
44. Andrea Rozzi, C. et al. Quantum coherence controls the charge separation in a prototypical artificial light-harvesting system. *Nat. Commun.* **4**, 1602 (2013).
45. Smith, S. L. & Chin, A. W. Phonon-assisted ultrafast charge separation in the PCBM band structure. *Phys. Rev. B* **91**, 201302 (2015).
46. Lee, C. K., Moix, J. & Cao, J. Coherent quantum transport in disordered systems: a unified polaron treatment of hopping and band-like transport. *J. Chem. Phys.* **142**, 164103 (2015).
47. Kato, A. & Ishizaki, A. Non-Markovian quantum-classical ratchet for ultrafast long-range electron-hole separation in condensed phases. *Phys. Rev. Lett.* **121**, 026001 (2018).
48. Tamura, H. & Burghardt, I. Ultrafast charge separation in organic photovoltaics enhanced by charge delocalization and vibronically hot exciton dissociation. *J. Am. Chem. Soc.* **135**, 16364–16367 (2013).
49. Tamura, H. & Burghardt, I. Potential barrier and excess energy for electron-hole separation from the charge-transfer exciton at donor-acceptor heterojunctions of organic solar cells. *J. Phys. Chem. C* **117**, 15020–15025 (2013).
50. Hughes, K. H., Cahier, B., Martinazzo, R., Tamura, H. & Burghardt, I. Non-Markovian reduced dynamics of ultrafast charge transfer at an oligothiophene-fullerene heterojunction. *Chem. Phys.* **442**, 111–118 (2014).
51. Chenel, A., Mangaud, E., Burghardt, I., Meier, C. & Desouter-Lecomte, M. Exciton dissociation at donor-acceptor heterojunctions: dynamics using the collective effective mode representation of the spin-boson model. *J. Chem. Phys.* **140**, 044104 (2014).
52. Huix-Rotllant, M., Tamura, H. & Burghardt, I. Concurrent effects of delocalization and internal conversion tune charge separation at regioregular polythiophene-fullerene heterojunctions. *J. Phys. Chem. Lett.* **6**, 1702–1708 (2015).
53. Chaudhuri, S. et al. Electron transfer assisted by vibronic coupling from multiple modes. *J. Chem. Theory Comput.* **13**, 6000–6009 (2017).
54. Polkehn, M., Tamura, H. & Burghardt, I. Impact of charge-transfer excitons in regioregular polythiophene on the charge separation at polythiophene-fullerene heterojunctions. *J. Phys. B* **51**, 014003 (2018).
55. Bian, Q. et al. Vibronic coherence contributes to photocurrent generation in organic semiconductor heterojunction diodes. *Nat. Commun.* **11**, 617 (2020).
56. Yao, Y., Xie, X. & Ma, H. Ultrafast long-range charge separation in organic photovoltaics: promotion by off-diagonal vibronic couplings and entropy increase. *J. Phys. Chem. Lett.* **7**, 4830–4835 (2016).

57. Duan, H. G., Jha, A., Tiwari, V., Miller, R. J. & Thorwart, M. Dissociation and localization dynamics of charge transfer excitons at a donor-acceptor interface. *Chem. Phys.* **528**, 110525 (2020).

58. Tamascelli, D., Smirne, A., Huelga, S. F. & Plenio, M. B. Nonperturbative treatment of non-markovian dynamics of open quantum systems. *Phys. Rev. Lett.* **120**, 30402 (2018).

59. Somoza, A. D., Marty, O., Lim, J., Huelga, S. F. & Plenio, M. B. Dissipation-assisted matrix product factorization. *Phys. Rev. Lett.* **123**, 100502 (2019).

60. Tamascelli, D., Smirne, A., Lim, J., Huelga, S. F. & Plenio, M. B. Efficient simulation of finite-temperature open quantum systems. *Phys. Rev. Lett.* **123**, 090402 (2019).

61. Mascherpa, F. et al. Optimized auxiliary oscillators for the simulation of general open quantum systems. *Phys. Rev. A* **101**, 052108 (2020).

62. Alvertis, A. M., Schröder, F. A. & Chin, A. W. Non-equilibrium relaxation of hot states in organic semiconductors: Impact of mode-selective excitation on charge transfer. *J. Chem. Phys.* **151**, 084104 (2019).

63. Gelinas, S. et al. Ultrafast long-range charge separation in organic semiconductor photovoltaic diodes. *Science* **343**, 512–516 (2014).

64. Deibel, C., Strobe, T. & Dyakonov, V. Role of the charge transfer state in organic donor-acceptor solar cells. *Adv. Mater.* **22**, 4097–4111 (2010).

65. Bakulin, A. A., Rao, A., Beljonne, D. & Friend, R. H. The role of driving energy and delocalized states for charge separation in organic semiconductors. *Science* **335**, 1340–1344 (2012).

66. Tamai, Y. et al. Ultrafast long-range charge separation in nonfullerene organic solar cells. *ACS Nanoacsnano* **11**, 12473–12481 (2017).

67. Nan, G., Zhang, X. & Lu, G. Do "hot" charge-transfer excitons promote free carrier generation in organic photovoltaics? *J. Phys. Chem. C.* **119**, 15028–15035 (2015).

68. Cheung, D. L. & Troisi, A. Theoretical study of the organic photovoltaic electron acceptor pcbm: morphology, electronic structure, and charge localization. *J. Phys. Chem. C* **114**, 20479–20488 (2010).

69. Idé, J., Fazzi, D., Casalegno, M., Meille, S. V. & Raos, G. Electron transport in crystalline PCBM-like fullerene derivatives: a comparative computational study. *J. Mater. Chem. C* **2**, 7313–7325 (2014).

70. Chen, X.-K. & Brédas, J. Voltage losses in organic solar cells: understanding the contributions of intramolecular vibrations to nonradiative recombinations. *Adv. Energy Mater.* **8**, 1702227 (2018).

71. Alvertis, A. M. & Engel, E. A. Importance of vibrational anharmonicity for electron-phonon coupling in molecular crystals. *Phys. Rev. B* **105**, L180301 (2022).

72. Raimbault, N., Athavale, V. & Rossi, M. Anharmonic effects in the low-frequency vibrational modes of aspirin and paracetamol crystals. *Phys. Rev. Mater.* **3**, 053605 (2019).

73. Menke, S. M. et al. Order enables efficient electron-hole separation at an organic heterojunction with a small energy loss. *Nat. Commun.* **9**, 277 (2018).

74. Hinrichsen, T. F. et al. Long-lived and disorder-free charge transfer states enable endothermic charge separation in efficient non-fullerene organic solar cells. *Nat. Commun.* **11**, 5617 (2020).

75. Gregg, B. A. Entropy of charge separation in organic photovoltaic cells: the benefit of higher dimensionality. *J. Phys. Chem. Lett.* **2**, 3013–3015 (2011).

76. Ono, S. & Ohno, K. Combined impact of entropy and carrier delocalization on charge transfer exciton dissociation at the donor-acceptor interface. *Phys. Rev. B* **94**, 075305 (2016).

77. Grancini, G. et al. Hot exciton dissociation in polymer solar cells. *Nat. Mater.* **12**, 29–33 (2013).

Author contributions

S.F.H., J.L., and M.B.P. conceived and initiated the project. A.S.M., N.L., and J.L. performed the numerical simulations. All authors discussed the results and contributed to the writing of the manuscript. The project was supervised by S.F.H. and M.B.P.

Competing interests

The authors declare no competing interests.

Additional information

Supplementary information The online version contains supplementary material available at https://doi.org/10.1038/s42005-023-01179-z.

Correspondence and requests for materials should be addressed to Alejandro D. Somoza or Martin B. Plenio.

Peer review information *Communications Physics* thanks Brendon Lovett and the other, anonymous, reviewer(s) for their contribution to the peer review of this work.

Reprints and permission information is available at http://www.nature.com/reprints

Publisher's note Springer Nature remains neutral with regard to jurisdictional claims in published maps and institutional affiliations.